

Computational Modeling of Hip Replacement Surgery: Total Hip Replacement vs. Hip Resurfacing

E. Kuhl & F. Balle

The motivation of the present work is the computational simulation of hip replacement surgery by means of a finite element approach based on open system thermodynamics. Its key feature is a non-constant material density, which is allowed to adapt with respect to changes in the mechanical loading environment. From a computational point of view, the density is treated as an internal variable. Its evolution is governed by a first order rate equation, the balance of mass, which is enhanced by an additional mass production term to account for growth. An implicit Euler backward scheme is suggested for its time discretization. The algorithmic determination of the material density based on a local Newton iteration is presented. To ensure quadratic convergence of the global Newton Raphson solution scheme, a consistent linearization of the discrete algorithmic equations is carried out. Finally, two alternative medical techniques in hip arthritis are compared, the conventional total hip replacement strategy and the more recent hip resurfacing technology. The result of the suggested remodeling algorithm is shown to agree remarkably well with clinically observed phenomena.

1 Motivation

Artificial joint replacement is a common surgical procedure with a relatively high success rate. In total hip replacement, the damaged upper end of the femur is replaced by a metal or ceramic ball attached to a metal stem fitted into the femur. In addition, a plastic or ceramic socket is implanted into the pelvis replacing the damaged socket. A typical prosthesis stem (DePuy Orthopaedics) is shown in figure 1. Depending on the age and activity of the patient, the prosthesis can either be anchored into the surrounding bone by a plastic bone cement or a cementless press fit implantation can be applied. Total hip replacement gives reasonably good results in elderly inactive people, but the long-term results are less promising in active young people. After surgical implantation, the muscle and joint loads are carried almost entirely by the stiff prosthesis stem, while the remaining part of the femur exhibits stress shielding. As a result, the patient typically suffers from long-term changes in bone architecture. These include increased bone formation in some regions, while other regions are characterized through bone resorption. Severe bone loss may cause painful loosening of the implant and ten to fifteen years post-operatively, a revision might become unavoidable.



Figure 1. Hip replacement prosthesis (DePuy)



Figure 2. Hip resurfacing prosthesis (MMT)

To overcome these problems, hip resurfacing was introduced and successfully applied worldwide since early nineties. In this relatively new kind of hip arthritis treatment, the ball of the femur is resurfaced with a metal shell rather than being removed and replaced. Accordingly, most of the patient's own bone is preserved and the anatomical loading situation is almost unaffected. Figure 2 shows a typical hip resurfacing prosthesis (Midland Mecial Technologies). Hip resurfacing restores normal function without any restriction of activities. In contrast to conventional total hip replacement, it minimizes invasive bone surgery and conserves as much intact bone as possible. Long-term stress shielding and the related loosening of the implant are thus avoided. Moreover, revision is much easier than in the classical treatment. Hip resurfacing thus seems to be the ideal option for the younger more active patient.

Since the mid eighties, finite element based numerical simulations have been carried out to improve the understanding of the functional adaptation of bone in response to changes in mechanical loading. In the underlying theories, the biological structure is considered as an open system which is allowed to constantly exchange mass with its environment. The first continuum theory in which the traditional balance of mass is supplemented by an additional source term dates back to the early work of Cowin and Hegedus (1976), see also Epstein and Maugin (2000) or Kuhl and Steinmann (2003a,b). From a numerical point of view, the enhanced balance of mass can either be solved globally next to the balance of momentum by introducing both, the density and the deformation as global degrees of freedom, or it can be solved locally on the integration point level. A systematic comparison of both approaches has been carried out by Jacobs et al. (1995), see also Kuhl et al. (2003). For the present purpose of bone remodeling around implants, we apply an integration point based approach which inherently accounts for discontinuous density distributions, see e.g. Harrigan and Hamilton (1992, 1993), Weng (1998), Nackenhurst (1997a,b) and Himpel (2003). In contrast to the original work by Beaupré et al. (1990), Carter et al. (1989), Huiskes et al. (1987) and Weinans et al. (1992), we apply an unconditionally stable Euler backward scheme for the temporal discretization of the balance of mass.

The basic aim of the present work is the numerical simulation of the long-time behavior of the proximal femur in response to hip resurfacing treatment as described in McMinn et al. (1996). To this end, density changes around the implanted metal shell are predicted and compared with those resulting from classical uncemented total hip replacement as simulated earlier e.g. by Huiskes et al. (1987), Weinans et al. (1994), Harrigan et al. (1996) and Nackenhurst (1997b). Before we illustrate the computational results, we briefly summarize the governing equations in section 2 and sketch the algorithmic treatment of the balance of mass in section 3. In section 4 we then compare the simulated post-operative response for the conventional total hip replacement with the new hip resurfacing technology. The proposed strategy and its future perspectives are finally discussed in section 5.

2 Continuum Theory of Growth

The underlying kinematic setting is characterized through the nonlinear motion $\varphi(\mathbf{X}, t) : \mathcal{B}_0 \times \mathbb{R} \rightarrow \mathcal{B}_t$ mapping material points \mathbf{X} in \mathcal{B}_0 onto spatial points $\mathbf{x} = \varphi(\mathbf{X}, t)$ in \mathcal{B}_t . Accordingly, the corresponding linear tangent map $\mathbf{F} = \nabla \varphi(\mathbf{X}, t) : T\mathcal{B}_0 \rightarrow T\mathcal{B}_t$ maps elements from the material tangent space $T\mathcal{B}_0$ to the spatial tangent space $T\mathcal{B}_t$. Moreover, we can introduce the right Cauchy–Green tensor $\mathbf{C} = \mathbf{F}^t \cdot \mathbf{g} \cdot \mathbf{F}$, i.e. the pull back of the covariant spatial metric \mathbf{g} , and the left Cauchy–Green tensor $\mathbf{b} = \mathbf{F} \cdot \mathbf{G}^{-1} \cdot \mathbf{F}^t$, i.e. the push forward of the contravariant material metric \mathbf{G}^{-1} , as characteristic strain measures. Let us assume that the volume specific free energy density ψ_0 can be expressed as the mass specific free energy density ψ weighted by the material density ρ_0 .

$$\psi_0 = \rho_0 \psi \quad \text{with} \quad \rho_0 = \rho_0(\mathbf{X}, t) \quad \text{and} \quad \psi = \psi(\rho_0, \mathbf{F}; \mathbf{X}) \quad (1)$$

In contrast to classical thermodynamics of closed systems, however, the material density ρ_0 is now no longer constant. Its evolution is governed by the balance of mass of open system thermodynamics,

$$d_t \rho_0 = \mathcal{R}_0 \quad \text{with} \quad \mathcal{R}_0 = c \left[\left[\frac{\rho_0}{\rho_0^*} \right]^{n-m} \psi_0^{\text{neo}} - \psi_0^* \right] \quad (2)$$

in which the righthand side \mathcal{R}_0 represents a mass source that accounts for growth. The constant c characterizes the speed of adaptation, n and m are two characteristic exponents, ρ_0^* is the reference density and ψ_0^* the reference free energy or rather the biological stimulus. This energy driven format of growth dates back to the work of Harrigan and Hamilton (1992, 1993) and was found to render a stable algorithmic formulation provided that $m > n$, see also Kuhl et al. (2003). Following the approach of Carter and Hayes (1977), the mass specific free energy density of cellular materials ψ can be introduced as the elastic free energy ψ^{neo} , e.g. of Neo–Hookean type, weighted by the relative density $[\rho_0 / \rho_0^*]^n$,

$$\psi = \left[\frac{\rho_0}{\rho_0^*} \right]^n \psi^{\text{neo}} \quad \text{with} \quad \psi^{\text{neo}} = \frac{1}{2\rho_0} \lambda \ln^2(J) + \frac{1}{2\rho_0} \mu [I_1 - n^{\text{dim}} - 2 \ln(J)] \quad (3)$$

see also Gibson and Ashby (1997). Again, $\psi_0^{\text{neo}} = \rho_0 \psi^{\text{neo}}$. For open pored cellular materials, the exponent n typically varies between $1 \leq n \leq 3.5$. As indicated in equation (3), the Neo–Hookean part of the free energy ψ^{neo} is given in terms of the first invariant $I_1 = \mathbf{C} : \mathbf{G}^{-1} = \mathbf{b} : \mathbf{g}$ and the Jacobian $J = \det(\mathbf{F})$, parameterized in terms of the two Lamé parameters λ and μ . Moreover, n^{dim} denotes the number of spatial dimensions. The free energy (3) defines the Kirchoff stress $\boldsymbol{\tau}$, i.e. the covariant push forward of the second Piola Kirchoff stress $\mathbf{S} = 2\rho_0 \partial_{\mathbf{C}} \psi$ as $\boldsymbol{\tau} = \mathbf{F} \cdot \mathbf{S} \cdot \mathbf{F}^t$ and thus

$$\boldsymbol{\tau} = \left[\frac{\rho_0}{\rho_0^*} \right]^n \boldsymbol{\tau}^{\text{neo}} \quad \text{with} \quad \boldsymbol{\tau}^{\text{neo}} = \mu \mathbf{b} + [\lambda \ln(J) - \mu] \mathbf{g}^{-1}. \quad (4)$$

Accordingly, the spatial Kirchhoff tangent \mathcal{C} relating the Lie derivative of the Kirchhoff stress $\mathcal{L}_t \boldsymbol{\tau}$ to the Lie derivative of the covariant spatial metric $\mathcal{L}_t \mathbf{g}$ as $\mathcal{L}_t \boldsymbol{\tau} = \mathcal{C} : \mathcal{L}_t \mathbf{g}/2$ is defined through the contravariant push forward $\mathcal{C} = [\mathbf{F} \otimes \mathbf{F}] : \mathcal{C}_0 : [\mathbf{F}^t \otimes \mathbf{F}^t]$ of the material tangent $\mathcal{C}_0 = 2 \, \text{d}_{\mathcal{C}} \mathcal{S}(\mathcal{C}, \rho_0) = 2 \, \partial_{\mathcal{C}} \mathcal{S} + 2 \, \partial_{\rho_0} \mathcal{S} \otimes \partial_{\mathcal{R}_0} \rho_0$. With the individual contributions $2 \, \partial_{\rho_0} \mathcal{S} \otimes \partial_{\mathcal{C}} \mathcal{R}_0 = n c [\rho_0 / \rho_0^*]^{[n-m]} / \rho_0 \mathcal{S} \otimes \mathcal{S}$ and $\partial_{\mathcal{R}_0} \rho_0 = [\partial_{\rho_0} \mathcal{R}_0]^{-1} = [c [n-m] [\rho_0 / \rho_0^*]^{[n-m]} \psi^{\text{neo}}]^{-1}$ it takes the following explicit representation.

$$\mathcal{C} = \left[\frac{\rho_0}{\rho_0^*} \right]^n \mathcal{C}^{\text{neo}} + \frac{n}{[n-m] \psi_0} \boldsymbol{\tau} \otimes \boldsymbol{\tau} \quad \text{with} \quad \mathcal{C}^{\text{neo}} = \lambda \mathbf{g}^{-1} \otimes \mathbf{g}^{-1} + [\mu - \lambda \ln(J)] \mathbf{i} \quad (5)$$

In the above equation, \mathbf{i} is the fourth order identity which can be expressed as $\mathbf{i} = [\mathbf{g}^{-1} \otimes \mathbf{g}^{-1} + \mathbf{g}^{-1} \otimes \mathbf{g}^{-1}] / 2$ by making use of the abbreviations \otimes and \otimes for the non-standard dyadic products according to the following component-wise definitions $\{\bullet \otimes \circ\}_{ijkl} = \{\bullet\}_{ik} \otimes \{\circ\}_{jl}$ and $\{\bullet \otimes \circ\}_{ijkl} = \{\bullet\}_{il} \otimes \{\circ\}_{jk}$.

3 Computational Modeling of Growth

The evolution of the material density ρ_0 is governed by the balance of mass (2), a first order rate equation which has to be discretized in time. To this end, we apply an unconditionally stable implicit Euler backward scheme based on the finite difference interpolation $\text{d}_t \rho_0 = [\rho_0^{n+1} - \rho_0^n] / \Delta t$ of the density evolution. The discrete counterpart of equation (2) can then be cast into the following residual statement $\mathbf{R} = c [[\rho_0^{n+1} / \rho_0^*]^{[n-m]} \psi_0^{\text{neo}} - \psi_0^*] \Delta t - \rho_0^{n+1} + \rho_0^n \doteq 0$ which is obviously a nonlinear equation in terms of the current density ρ_0^{n+1} . We thus suggest an iterative solution strategy based on a local Newton iteration such that $\mathbf{R}_{k+1} = \mathbf{R}_k + \text{d}\mathbf{R}_k \Delta \rho_0 \doteq 0$. The linearization of the residual $\text{d}\mathbf{R}_k = \partial_{\rho_0^{n+1}} \mathbf{R}_k = c [n-m] [\rho_0^{n+1} / \rho_0^*]^{[n-m]} \psi^{\text{neo}} \Delta t - 1$ renders the incremental update of the density as $\Delta \rho_0 = -\mathbf{R}_k / \text{d}\mathbf{R}_k$. The material density can then be updated as $\rho_0^{n+1} \leftarrow \rho_0^{n+1} + \Delta \rho_0$. Recall that in the algorithmic context, the continuous fourth order tangent operator \mathcal{C} introduced in equation (5) has to be replaced by its algorithmic counterpart

$$\mathcal{C}^{\text{alg}} = \left[\frac{\rho_0}{\rho_0^*} \right]^n \mathcal{C}^{\text{neo}} + \frac{c n [\rho_0 / \rho_0^*]^{-m}}{\rho_0 - c [n-m] [\rho_0 / \rho_0^*]^{[n-m]} \psi_0^{\text{neo}} \Delta t} \boldsymbol{\tau} \otimes \boldsymbol{\tau}$$

to ensure quadratic convergence of the global Newton iteration. The algorithmic tangent operator \mathcal{C}^{alg} follows straightforwardly from the consistent linearization of the time discrete set of equations on the basis of the Euler backward time integration scheme as summarized in table 1.

compute elastic free energy	$\psi^{\text{neo}} = \lambda \ln^2(J^{n+1}) / 2\rho_0 + \mu [I_1^{n+1} - n^{\text{dim}} - 2 \ln(J^{n+1})] / 2\rho_0$
compute elastic stress	$\boldsymbol{\tau}^{\text{neo}} = \mu \mathbf{b}^{n+1} + [\lambda \ln(J^{n+1}) - \mu] \mathbf{g}^{-1}$
compute elastic tangent	$\mathcal{C}^{\text{neo}} = \lambda \mathbf{g}^{-1} \otimes \mathbf{g}^{-1} + [\mu - \lambda \ln(J^{n+1})] \mathbf{i}$
local Newton iteration	
compute residual	$\mathbf{R} = c [[\rho_0^{n+1} / \rho_0^*]^{[n-m]} \rho_0^{n+1} \psi^{\text{neo}} - \psi_0^*] \Delta t - \rho_0^{n+1} + \rho_0^n$
compute derivative	$\text{d}\mathbf{R} = c [n-m] [\rho_0^{n+1} / \rho_0^*]^{[n-m]} \psi^{\text{neo}} \Delta t - 1$
compute incremental update	$\Delta \rho_0 = -\mathbf{R} / \text{d}\mathbf{R}$
update reference density	$\rho_0^{n+1} \leftarrow \rho_0^{n+1} + \Delta \rho_0$
check convergence	$ \Delta \rho_0 \leq \text{tol}$
compute growth stress	$\boldsymbol{\tau}^{n+1} = [\rho_0^{n+1} / \rho_0^*]^n \boldsymbol{\tau}^{\text{neo}}$
compute growth tangent	$\mathcal{C}^{n+1} = [\rho_0^{n+1} / \rho_0^*]^n \mathcal{C}^{\text{neo}} - c n / \rho_0^{n+1} [\rho_0^{n+1} / \rho_0^*]^{-m} / \text{d}\mathbf{R} \boldsymbol{\tau}^{n+1} \otimes \boldsymbol{\tau}^{n+1}$

Table 1: Algorithmic formulation of growth

4 Functional Adaptation in Hip Replacement Surgery

Finally, the suggested algorithm is applied to predict the density distribution in the proxima femur. The femur geometry and the applied set of loading are depicted in figure 3. Within the present study, we shall restrict ourselves to a two dimensional setting keeping in mind that biologically relevant torsional effects are thus neglected. As far as the suggested finite element model is concerned, the extension to the realistic three dimensional case is straightforward. However, as documented e.g. by Bergmann et al. (2001), the three dimensional loading situation

is still not entirely clarified. Fortunately, there is a huge body of literature on the two dimensional loading situation, for which three representative load cases can be identified, see e.g. Carter and Beaupré (2001). Load case 1 corresponds to the load condition for the midstance phase of gait, while load cases 2 and 3 represent the extreme cases of abduction and adduction as defined in table 2. Following the literature, all loads are applied as concentrated point loads. In what follows, a superposition of all three load cases is applied in order to represent an average daily loading situation.

The outer shaft is assumed to consist of cancellous bone with a Young's modulus of $E = 16000$ MPa and Poisson's ratio of $\nu = 0.3$, corresponding to the Lamé constants $\lambda = 6153.8$ and $\mu = 6153.8$, compare the shaded areas around the femur stem in figure 3. The spongy bone which covers the remaining areas is modeled with a Young's modulus of $E = 2000$ MPa and Poisson's ratio of $\nu = 0.3$, i.e. $\lambda = 769.2$ and $\mu = 769.2$. Both are assumed to have a similar density of $\rho_0^* = 1.2$ g/cm³ which is the average value of spongy bone with $\rho_0^* \approx 0.60$ g/cm³ and cortical bone with $\rho_0^* \approx 1.80$ g/cm³. Yet a number of case studies has shown that the initial density ρ_0^* does not have a significant influence on the final density distribution, see Balle (2004). The parameters of the growth law have been chosen as $\psi_0^* = 0.01$, $n = 2$, $m = 3$ and $c = 1$, see e.g. Nackenhörst (1997a).

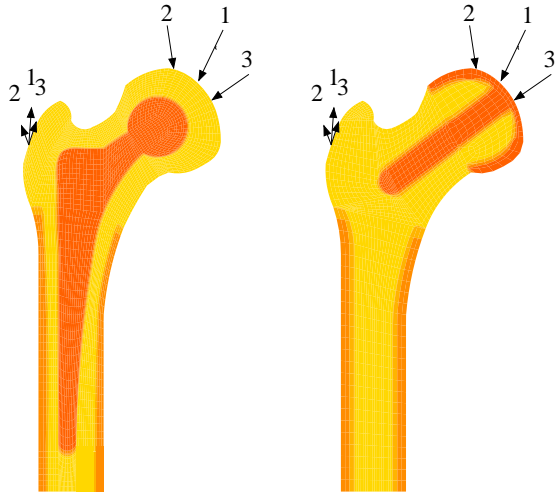


Figure 3. Femur – Load cases 1, 2 and 3

100 time steps of $\Delta t = 2$ each have been calculated to obtain a state of biological equilibrium in which the density distribution has converged towards a stable state in response to the applied loading, i.e. $d_t \rho_0 = 0$ everywhere. Once the normal bone architecture has been generated, a virtual implantation of the prosthesis can be performed by replacing the material properties of the red bone elements in figure 3 by those of the implant. We assume a titanium prosthesis of type Ti6Al7Nb with $E = 110000$ MPa and $\nu = 0.3$, i.e. $\lambda = 42307.7$ and $\mu = 42307.7$. We then calculate 100 post-operative time steps until the final biological equilibrium state is reached. Within the present study, we focus on the comparison of two different medical treatments, i.e. the conventional total hip replacement and the more recent hip resurfacing technology. Additional parameter studies providing further insight into the functional adaptation in the proxima femur can be found in Balle (2004).

load case	type of loading	joint force	load angle	muscle force	load angle
1	midstance phase of gait	2.317 kN	24 ⁰	0.703 kN	28 ⁰
2	extreme range of abduction	1.158 kN	-15 ⁰	0.351 kN	-8 ⁰
3	extreme range of adduction	1.548 kN	56 ⁰	0.468 kN	35 ⁰

Table 2: Femur – Loading conditions

The resulting nonlinear system of equations is solved with the help of the Newton Raphson solution technique based on the algorithmic linearization of the governing equations as introduced in table 1. The efficiency of the numerical solution technique is highlighted by the quadratic convergence of the Newton Raphson scheme documented for four representative time steps in table 3. The convergence towards a biological equilibrium state is also obvious from this table as the initial residual of the first line reduces considerably with time.

residual	time step 1	time step 2	time step 10	time step 100
iteration 0	3.35185E+00	7.71671E-01	1.27550E-01	2.13553E-03
iteration 1	1.97183E+00	4.03076E-02	4.40137E-04	1.88447E-07
iteration 2	2.44517E-01	1.75829E-04	4.81531E-09	3.59574E-12
iteration 3	7.39790E-03	4.86157E-09	2.80950E-12	equilibrium
iteration 4	1.04351E-05	3.16634E-12	equilibrium	equilibrium
iteration 5	2.17531E-11	equilibrium	equilibrium	equilibrium

Table 3: Characteristic quadratic convergence of underlying Newton Raphson iteration scheme

4.1 Conventional Total Hip Replacement

To predict the density distribution after conventional total hip surgery, the proxima femur is discretized with 3812 standard four noded displacement elements. Note, however, that a coarsening of the mesh, e.g. a simulation with 953 elements, did not yield significantly different results, see Balle (2004). Figure 4, top row, depicts the underlying finite element mesh and the evolution of the density in the healthy bone. Convergence towards biological equilibrium is reached after approximately 75 time steps. The final density distribution at $t = 100$ shows the characteristic features of a healthy femur, i.e. the development of a dense system of compressive trabeculae carrying the stress from the superior contact surface to the calcar region of the medial cortex, a secondary arc system of trabeculae through the infero-medial joint surface into the lateral metaphyseal region, the formation of Ward's triangle as an area of low density and the development of a dense cortical shaft around the medullary core. In the femur shaft, the density is reduced by $[\rho_0 - \rho_0^*]/\rho_0^* = -0.3$. Having assumed an initial density of $\rho_0^* = 1.20 \text{ g/cm}^3$, we thus find a final material density of 0.84 g/cm^3 which agrees nicely with the value of $0.60 \pm 0.20 \text{ g/cm}^3$ as determined experimentally by Knauss (1980).

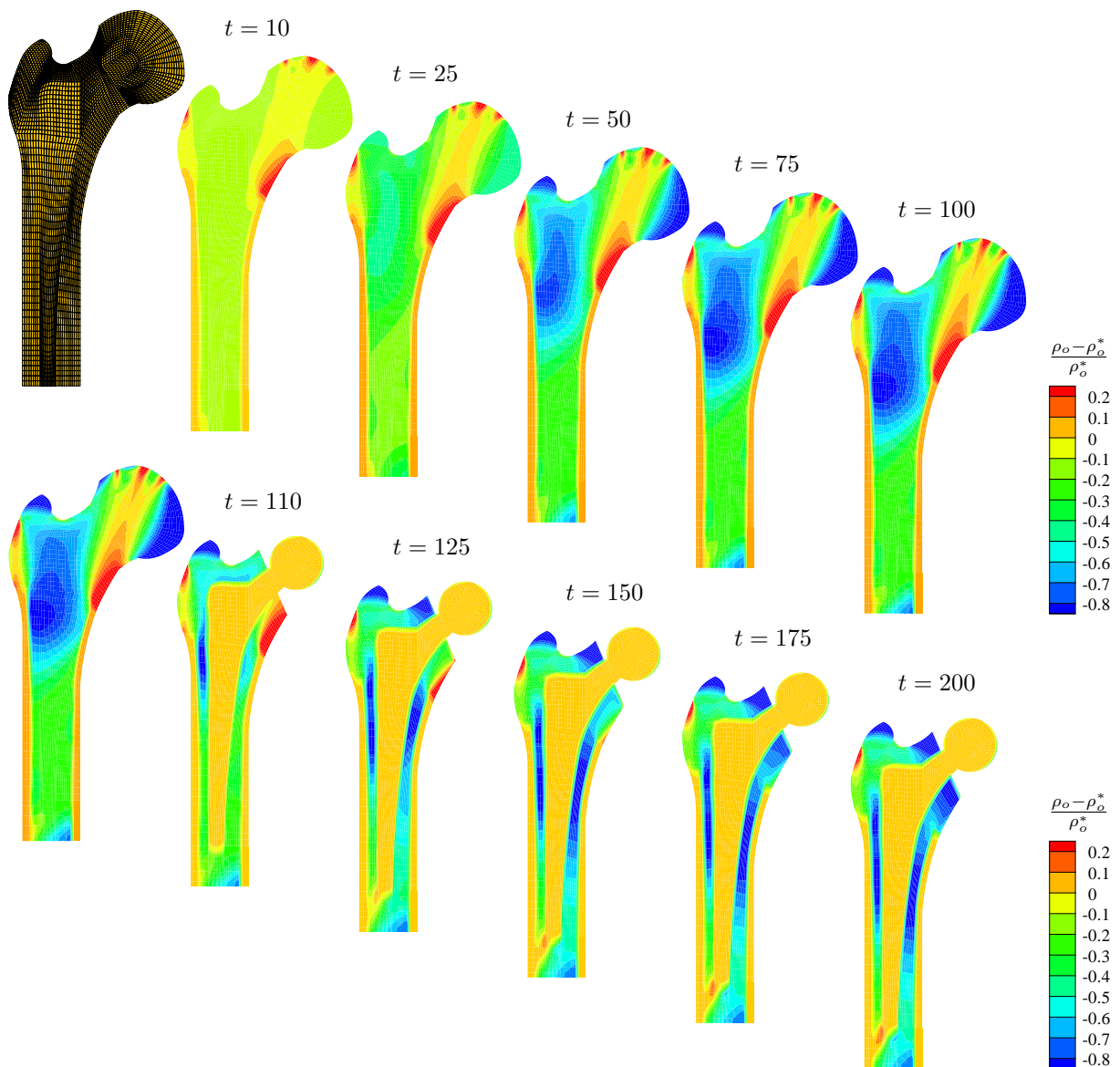


Figure 4. Density evolution in healthy bone and after conventional total hip replacement

Next, we carry out a virtual implantation of a traditional prosthesis by replacing the material properties of the red bone elements in figure 3, left, by those of the implant. The simulation of remodeling around the rigidly fixed femoral component of the implant predicts the classical pattern of remodeling characteristic for artificial joint replacement in most patients. The stiff titanium implant tends to transfer much of the joint forces down the

diaphysis to the distal portion of the implant stem, see figure 4, bottom row. At the distal tip of the stem, forces are transferred to the outer bone shaft. The resulting high stress concentration induces a pronounced deposition of bone mass at the distal tip of the prosthesis. Almost the entire loading is now carried by the stiff prosthesis stem. Accordingly, the proximal regions of the femur experience stress shielding resulting in a local net resorption of bone. As a long-term effect of this remodeling process, the patient typically suffers from aseptic loosening of the implant, in particular around the stiff prosthesis stem.

4.2 New Hip Resurfacing

Next, we elaborate the density redistribution in response to hip resurfacing. The proximal femur is now discretized with 1561 four noded displacement elements and the initial density distribution is generated similar to the previous example, compare figure 5, top row. Convergence towards the biological equilibrium state showing the characteristic features of the previous example is found after approximately 75 time steps. Although the results are, of course, similar to the healthy bone response in the previous example, this new generation of the initial state is necessary since the different geometry of the implant has to be taken into account a priori through a modified initial discretization.

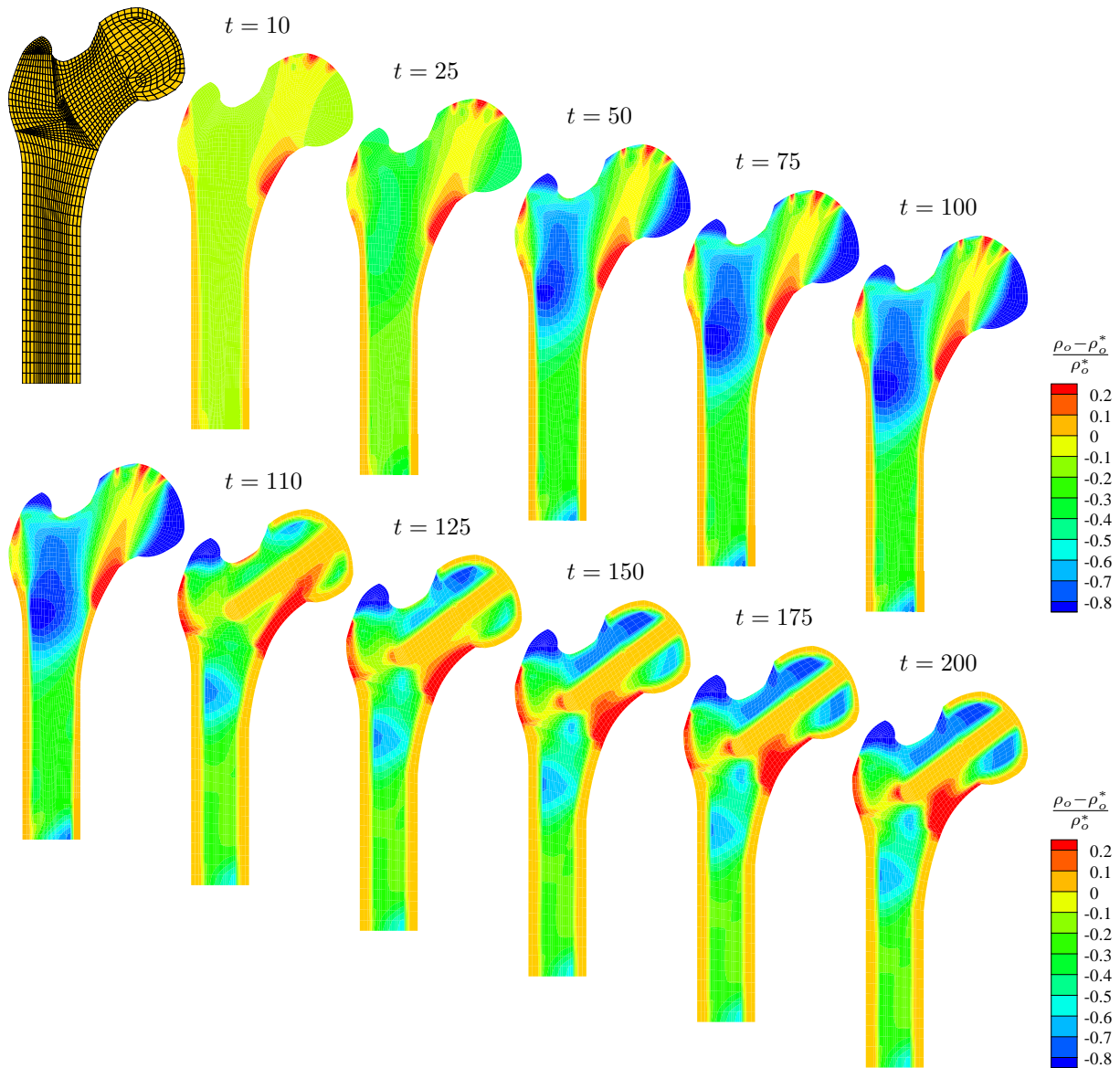


Figure 5. Density evolution in healthy bone and after new hip resurfacing

Once the density distribution of the healthy bone has been generated, virtual hip resurfacing can be carried out at time step $t = 101$ by taking into account the implant geometry introduced in figure 3, right. Figure 5, bottom row, shows the density redistribution in response to the new loading situation. A remarkable distal ingrowth of the nail shaped implant can be observed. Additional bone material is deposited locally with the aim of fixing the implant stem on the medial side. In addition, a lateral increase of bone mass can be observed starting locally at the stem tip. At the final equilibrium state, i.e. 100 time steps post-implantation, the implant stem is almost entirely fixed. However, in contrast to the conventional total hip replacement, the anatomical loading situation has not changed significantly. No bone resorption can be observed in the distal femur. The post-operative density distribution in the femur shaft is obviously almost identical to the anatomical situation before the implantation. The present simulation nicely illustrates the capability of the new hip resurfacing technology to restore normal function and bone architecture.

It should be mentioned, that in the present two dimensional study, bone resorption can be observed locally underneath the metallic shell. Since hip resurfacing is a relatively new medical treatment, we were not able to find reliable long-time case studies to verify this phenomenon. We assume that the numerically observed local density resorption is indeed a realistic effect, which is, however, most probably less pronounced in a fully three dimensional simulation. In the elderly inactive population, which form the vast majority of hip arthroplasty patients, hip resurfacing is thus neither indicated nor desirable on account of osteoporosis and the remaining risk of femoral head fracture.

5 Discussion

In the present manuscript, we have discussed a computationally efficient and numerically stable remodeling algorithm which allows to predict the functional adaptation of bone in response to changes in mechanical loading. The algorithm has been applied to the functional adaptation in response to hip replacement surgery. In the suggested approach, which falls into the framework of open system thermodynamics, changes in density are governed by the balance of mass supplemented by an additional mass source. This enhanced balance of mass is solved locally on the integration point level and the non-constant material density is introduced as an internal variable. Its evolution equation is discretized in time with an implicit Euler backward scheme. The algorithmic realization is supplemented by a consistent linearization ensuring quadratic convergence of the underlying Newton Raphson solution technique.

The numerical simulations of the conventional total hip replacement agree nicely with the long-term response in hip replacement surgery. The simulations of the hip resurfacing technology revealed the predicted advantages of this relatively new approach. In particular, it was shown to restore normal anatomy and avoid undesired stress shielding, bone resorption and painful implant loosening. Unlike in conventional hip replacement, ingrowth of the implant is not restricted to the lateral side. Rather, both sides of the implant are fixed by local deposition of bio-material after hip resurfacing treatment. The simulations of both types of medical treatment are in good qualitative agreement with clinical observations. Although the model has already been implemented into a three dimensional finite element framework, only two dimensional analyses have been discussed in the present study. The analyses of three dimensional remodeling phenomena is part of current research. Although this extension is straightforward in principle, it requires not only an increased computer power but also a detailed knowledge of the three dimensional loading situation which is unfortunately not yet characterized in a satisfactory way.

In the present model, changes in density are induced by mechanical loading alone. For the case of bone remodeling around implants, the related simulations seem to be in surprisingly good agreement with experimental findings. To apply the suggested approach in patient specific medical treatment, however, the model would also have to account for individual biological influence factors such as age, bone quality, nutrition etc. which certainly influence the turnover rate and the overall potential of adaptation. Nevertheless, we believe, that the present algorithm provides a promising numerical tool which serves to gain additional insight in mechanically induced bone remodeling. As such, it can not only be applied to optimize the mechanical properties of new implants or to generate optimal implant geometries but also to virtually predict the patient specific response to alternative medical strategies.

References

- Balle, F.: Biomechanische Untersuchungen zur Knochen–Implantat–Interaktion mit Hilfe der Methode der Finiten Elemente. *Diploma Thesis, LTM, University of Kaiserslautern*, U04–01.
- Beaupré, G. S.; Orr, T. E.; Carter, D. R.: An approach for time–dependent bone modelling and remodelling. *J. Orthop. Res.*, 8, (1990), 651–670.
- Bergmann, G., G. and Deuretzbacher; Heller, M.; Graichen, F.; Rohlmann, A.; Strauss, J.; Duda, G. N.: Hip contact forces and gait patterns from routine activities. *J. Biomechanics*, 34, (2001), 859–871.

- Carter, D. R.; Beaupré, G. S.: *Skeletal Function and Form – Mechanobiology of Skeletal Development, Aging and Regeneration*. Cambridge University Press (2001).
- Carter, D. R.; Hayes, W. C.: The behavior of bone as a two-phase porous structure. *J. Bone Jt. Surgery*, 59-A, (1977), 785–794.
- Carter, D. R.; Orr, T. E.; Fhyrie, D. P.: Relationships between loading history and femoral cancellous bone architecture. *J. Biomechanics*, 22, (1989), 231–244.
- Cowin, S. C.; Hegedus, D. H.: Bone remodelling I: Theory of adaptive elasticity. *J. Elasticity*, 6, (1976), 313–326.
- Epstein, M.; Maugin, G. A.: Thermomechanics of volumetric growth in uniform bodies. *Int. J. Plasticity*, 16, (2000), 951–978.
- Gibson, L. J.; Ashby, M. F.: *Cellular Solids*. Cambridge University Press, 2nd edn. (1997).
- Harrigan, T. P.; Hamilton, J. J.: Optimality condition for finite element simulation of adaptive bone remodeling. *Int. J. Solids & Structures*, 29, (1992), 2897–2906.
- Harrigan, T. P.; Hamilton, J. J.: Finite element simulation of adaptive bone remodelling: A stability criterion and a time stepping method. *Int. J. Num. Meth. Eng.*, 36, (1993), 837–854.
- Harrigan, T. P.; Hamilton, J. J.; Reuben, J. D.; Tone, A.; Viceconti, M.: Bone remodelling adjacent to intramedullary stems: An optimal structures approach. *Biomaterials*, 17, (1996), 223–232.
- Himpel, G.: On the modeling of material growth in anisotropic solids. Internal variable approach and numerical implementation. *Diploma Thesis, Institute of Applied Mechanics, University of Stuttgart*, 03-I-08.
- Huiskes, R.; Weinans, H.; Grootenboer, H. J.; Dalstra, M.; Fudala, B.; Slooff, T. J.: Adaptive bone-remodeling theory applied to prosthetic-design analysis. *J. Biomechanics*, 20, (1987), 1135–1150.
- Jacobs, C. R.; Levenston, M. E.; Beaupré, G. S.; Simo, J. C.; Carter, D. R.: Numerical instabilities in bone remodeling simulations: The advantages of a node-based finite element approach. *J. Biomechanics*, 28, (1995), 449–459.
- Knauss, P.: *Materialkennwerte und Festigkeitsverhalten des spongiösen und kompakten Knochengewebes am coxalen Human-Femur*. Ph.D. thesis, University of Stuttgart, Stuttgart, Germany (1980).
- Kuhl, E.; Menzel, A.; Steinmann, P.: Computational modeling of growth: A critical review, a classification of concepts and two new consistent approaches. *Comp. Mech.*, 32, (2003), 71–88.
- Kuhl, E.; Steinmann, P.: Mass- and volume specific views on thermodynamics for open systems. *Proceedings of the Royal Society of London*, 459, (2003a), 2547–2568.
- Kuhl, E.; Steinmann, P.: Theory and numerics of geometrically non-linear open system mechanics. *Int. J. Num. Meth. Eng.*, 58, (2003b), 1593–1615.
- McMinn, D.; Treacy, R.; Lin, K.; Pynsent, P.: Metal on metal surface replacement of the hip. *Clin. Orth. Rel. Res.*, 329, (1996), 89–98.
- Nackendorst, U.: Ein effizientes Finite Element Verfahren zur Simulation des beanspruchungsadaptiven Knochenwachstums. In: *Die Methode der Finiten Elemente in der Biomechanik, Biomedizin und angrenzenden Gebieten*, Workshop 1997, Universität Ulm (1997a).
- Nackendorst, U.: Numerical simulations of stress stimulated bone remodeling. *Technische Mechanik*, 17, (1997b), 31–40.
- Weinans, H.; Huiskes, R.; Grootenboer, H. J.: The behavior of adaptive bone-remodeling simulation models. *J. Biomechanics*, 25, (1992), 1425–1441.
- Weinans, H.; Huiskes, R.; Grootenboer, H. J.: Effects of fit and bonding characteristics of femoral stems on adaptive bone remodeling. *J. Biomech. Eng.*, 116, (1994), 393–400.
- Weng, S.: Ein anisotropes Knochenbaummodell und dessen Anwendung. *Technische Mechanik*, 18, (1998), 173–180.

Address: Ellen Kuhl, Chair for Applied Mechanics, TU Kaiserslautern, D-67653 Kaiserslautern; Frank Balle, Institute of Materials Science and Engineering, TU Kaiserslautern, D-67653 Kaiserslautern
email: ekuhl@rhrk.uni-kl.de; balle@mv.uni-kl.de.